

## Construction of a Highly Efficient MoS<sub>2</sub>-Based Composite Electrocatalyst for the Oxygen Evolution Reaction

Mengyan Huang<sup>a</sup>, Bo Liu<sup>d</sup>, Junwei Wu<sup>a</sup>, Junfeng Gu<sup>b</sup>, Yichen Zheng, Peiyan Ma<sup>a</sup>, \*, Bei Li<sup>d,\*</sup>, and Zhengyi Fu<sup>b,c,\*</sup>

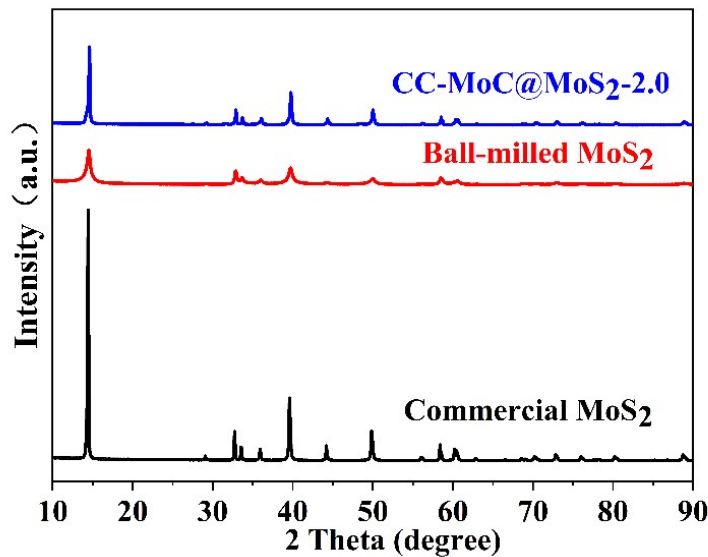


Fig. S1 XRD patterns of commercial MoS<sub>2</sub>, BM-MoS<sub>2</sub> and CC-MoC@MoS<sub>2</sub>-2.0.

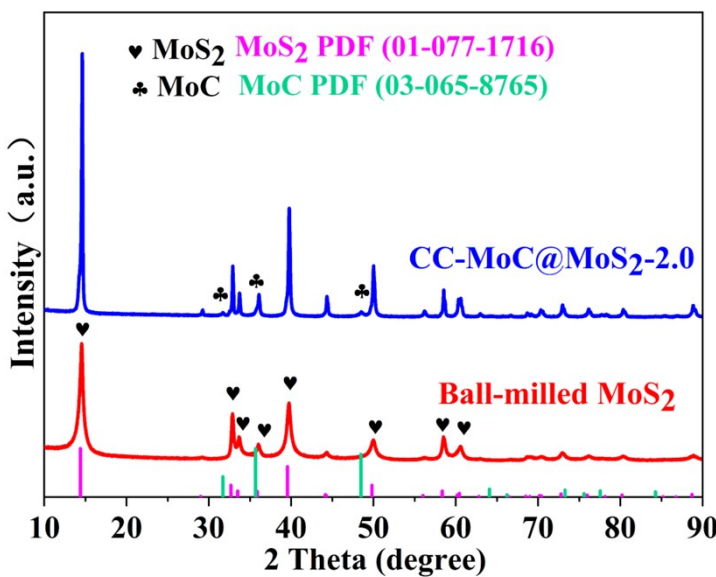
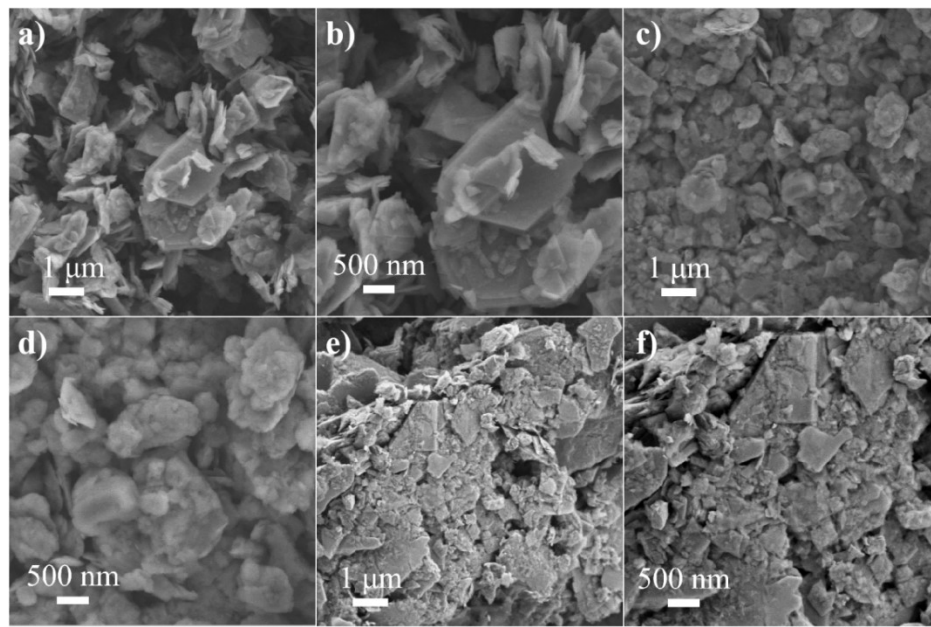
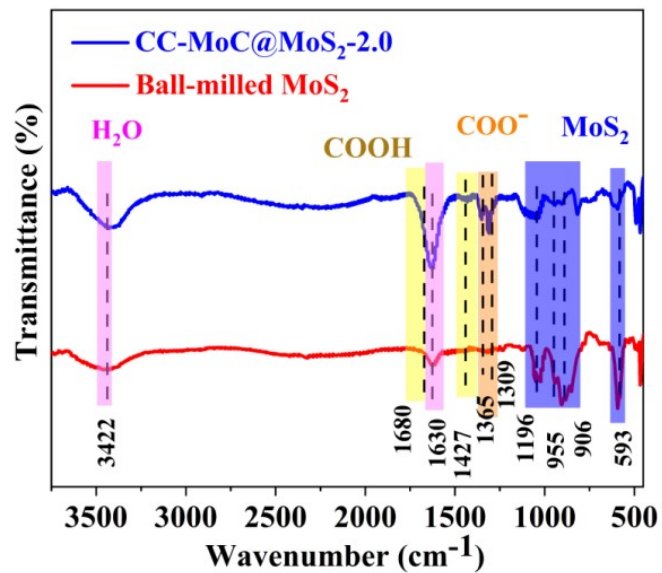


Fig. S2 XRD patterns of BM-MoS<sub>2</sub> and CC-MoC@MoS<sub>2</sub>-2.0.



**Fig. S3** SEM images of (a, b) commercial MoS<sub>2</sub>, (c, d) BM-MoS<sub>2</sub>, and (e, f) CC-MoC@MoS<sub>2</sub>-2.0.



**Fig. S4** FTIR spectra of BM-MoS<sub>2</sub> and CC-MoC@MoS<sub>2</sub>-2.0.

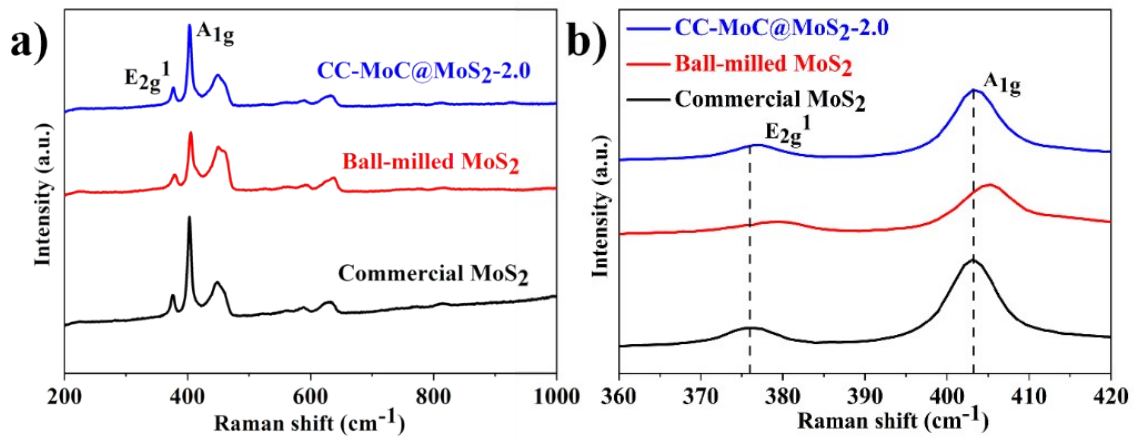


**Fig. S5** Raman spectra of commercial MoS<sub>2</sub>, BM-MoS<sub>2</sub> and CC-MoC@MoS<sub>2</sub>-2.0.

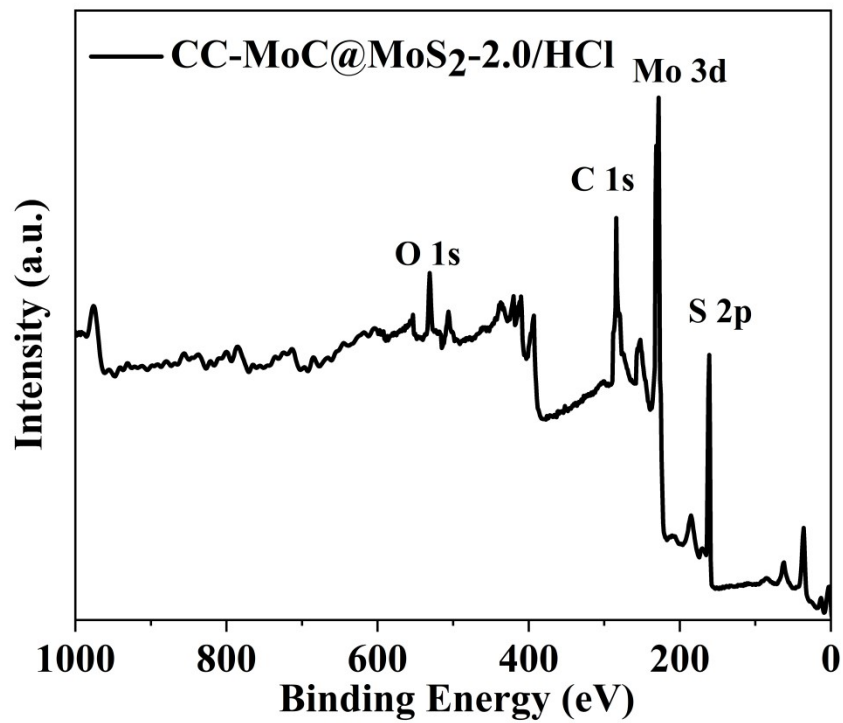


**Fig. S6** XPS survey scan of CC-MoC@MoS<sub>2</sub>-2.0 after treatment in 1.0 M HCl. The S/Mo ratio is 1.7.

**Table S1:** Elemental composition (mole %) of BM-MoS<sub>2</sub> and CC-MoC@MoS<sub>2</sub>-2.0 before and after treatment in 1.0 M HCl.

	Mo	S	C	O	S/Mo
Ball-milled MoS <sub>2</sub>	24.94%	50.28%	1.60%	23.18%	2.0
CC-MoC@MoS <sub>2</sub> -2.0	28.51%	40.24%	10.71%	20.54%	1.4
CC-MoC@MoS <sub>2</sub> -2.0 after HCl treatment	26.98%	45.87%	11.37%	15.78%	1.7

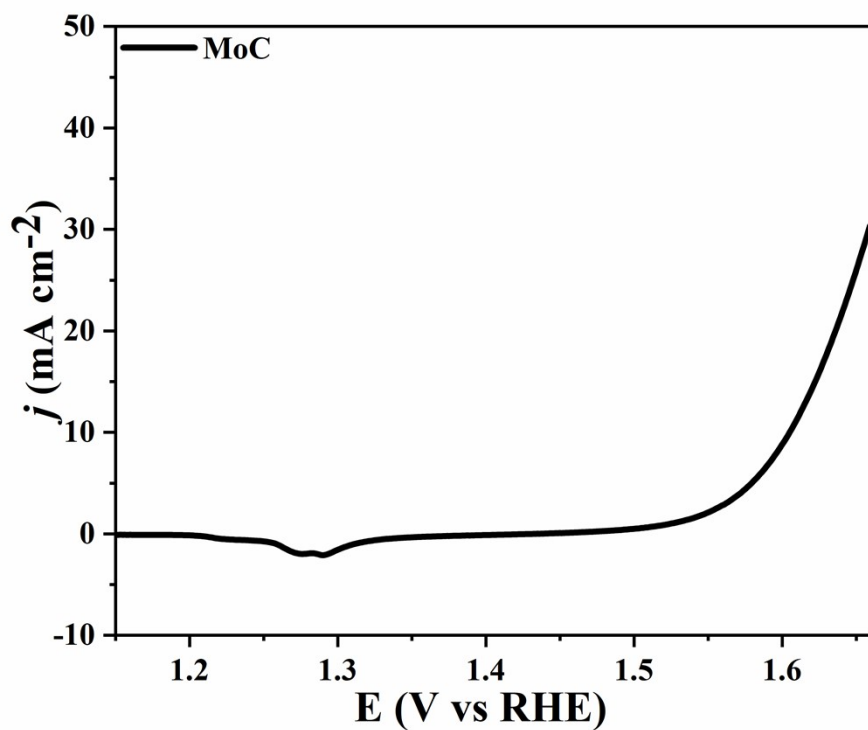


**Fig. S7** LSV curves of MoC supported on nickel foam for OER.

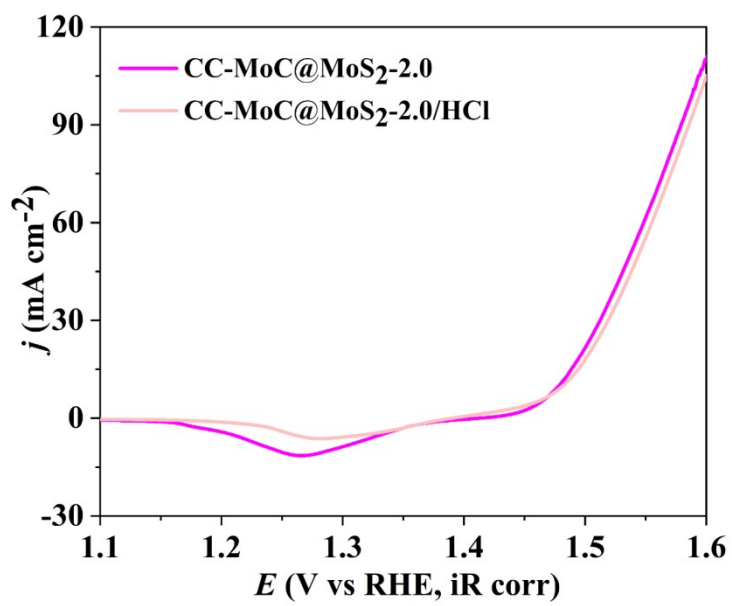


**Fig. S8** LSV curves of CC-MoC@MoS<sub>2</sub>-2.0 before and after acid treatment (1.0 M HCl).

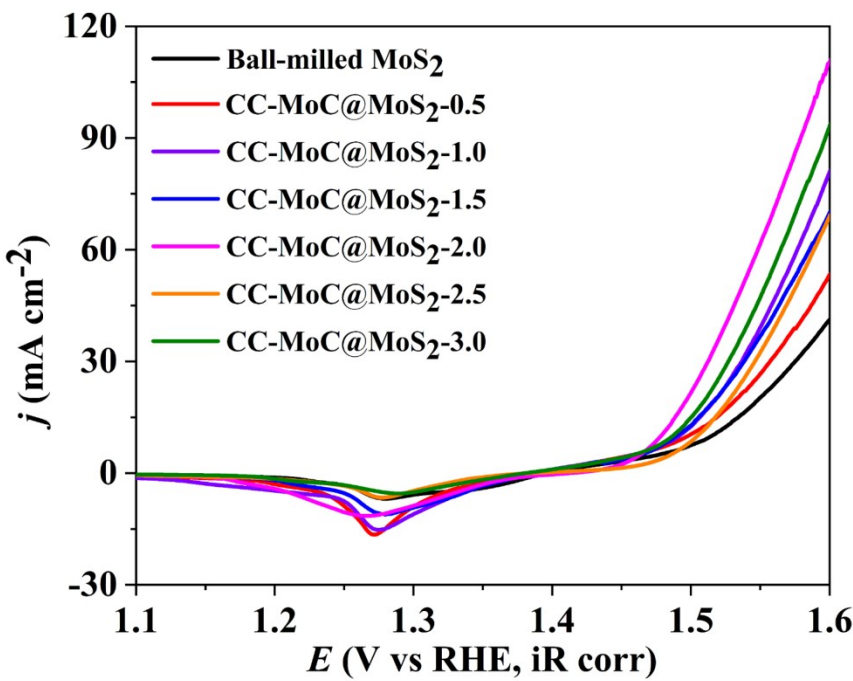


**Fig. S9** OER polarization curves of BM-MoS<sub>2</sub>, CC-MoC@MoS<sub>2</sub>-0.5, CC-MoC@MoS<sub>2</sub>-1.0, CC-MoC@MoS<sub>2</sub>-1.5, CC-MoC@MoS<sub>2</sub>-2.0, CC-MoC@MoS<sub>2</sub>-2.5 and CC-MoC@MoS<sub>2</sub>-3.0.

**Table S2:** Comparison of the OER performance of CC-MoC@MoS<sub>2</sub>-2.0 with that of reported electrocatalysts (in 1M KOH).

Catalysts	$\eta_{10}$ (mV)	Tafel slope (mV dec <sup>-1</sup> )	$C_{dl}$ (mF cm <sup>-2</sup> )	$R_{ct}$ ( $\Omega$ )	Refs
CC-MoC@MoS <sub>2</sub> -2.0	248	47.09	4.02	0.716	This work
Fe <sub>3</sub> O <sub>4</sub> /CoO CNTs	270	59	30.07	17.5	[1]
Fe <sub>5</sub> Co <sub>4</sub> Ni <sub>20</sub> Se <sub>36</sub> B <sub>x</sub>	279.8	59.5	3.25	1.586	[2]
p Ni <sub>0.7</sub> Co <sub>0.3</sub> Se <sub>2</sub> Ns	258	42.3	0.04	32.8	[3]
Fe-NiO <sub>x</sub> NT	310	49	22.73	14.4	[4]
Ni <sub>2</sub> P NPs	290	47	0.176	1.8	[5]
Co-Ni-Fe <sub>511</sub> Ns	288	43	0.475	/	[6]
MnO <sub>2</sub> -CoP <sub>3</sub>	288	65	0.091	/	[7]
Fe <sub>3</sub> C@NCNTs-NCNFs	284	56	28.2	/	[8]
Fe <sub>3</sub> O <sub>4</sub> -Co <sub>3</sub> S <sub>4</sub> NS	260	56	63.2	/	[9]

NiFeMn LDH	262	47	2.466	/	[10]
Co, Nb-MoS <sub>2</sub> /TiO <sub>2</sub>	260.1	65	23.7	0.77	[11]
CoP/CN@MoS <sub>2</sub>	289	69	94.7	17	[12]
CoO <sub>x</sub> -MoC/NC	330	89.8	257	/	[13]
Co <sub>9</sub> S <sub>8</sub> -CuS-FeS	300	79	1.51	26	[14]
Ag@CoOOH	256	64.6	/	2.9	[15]
Carboxyl coordinated Ni/Co	258	76.5	/	/	[16]
Co <sub>6</sub> Mo <sub>6</sub> C <sub>2</sub> -NC-rGO	260	50	42	9	[17]

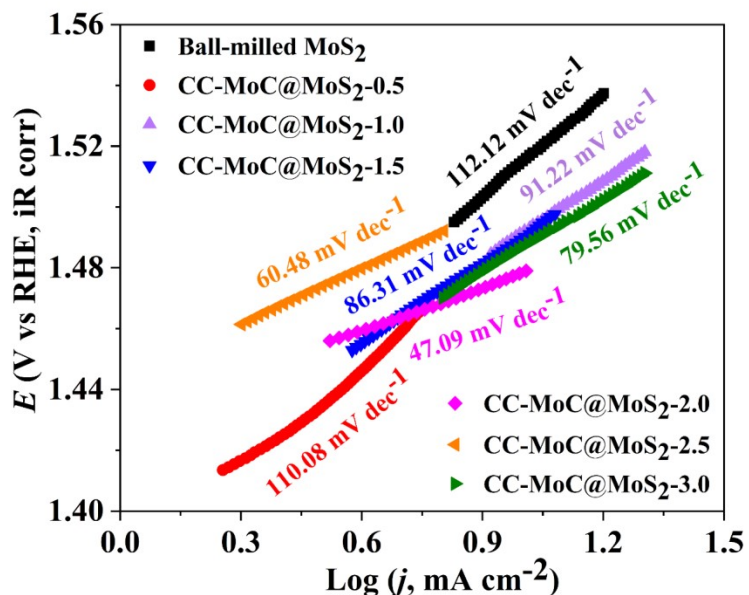


**Fig. S10** Tafel slopes of BM-MoS<sub>2</sub>, CC-MoC@MoS<sub>2</sub>-0.5, CC-MoC@MoS<sub>2</sub>-1.0, CC-MoC@MoS<sub>2</sub>-1.5, CC-MoC@MoS<sub>2</sub>-2.0, CC-MoC@MoS<sub>2</sub>-2.5 and CC-MoC@MoS<sub>2</sub>-3.0.

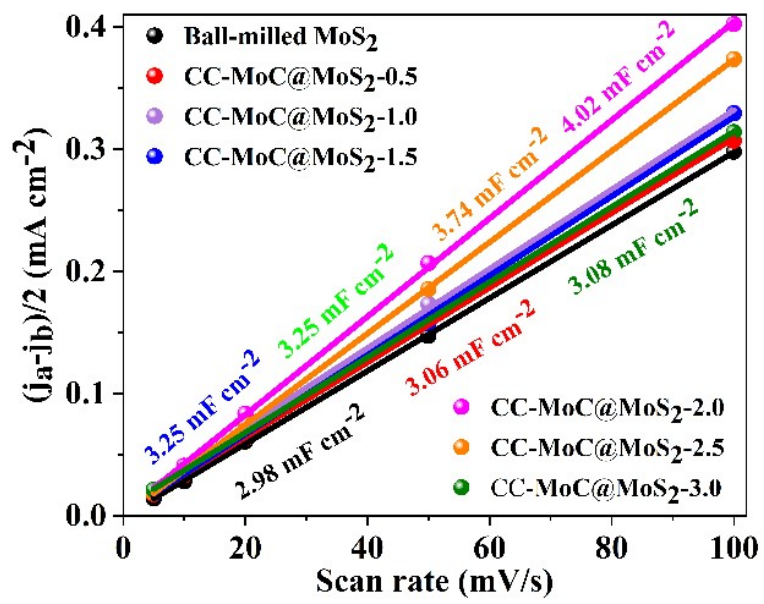


**Fig. S11**  $C_{dl}$  of BM-MoS<sub>2</sub>, CC-MoC@MoS<sub>2</sub>-0.5, CC-MoC@MoS<sub>2</sub>-1.0, CC-MoC@MoS<sub>2</sub>-1.5, CC-MoC@MoS<sub>2</sub>-2.0, CC-MoC@MoS<sub>2</sub>-2.5 and CC-MoC@MoS<sub>2</sub>-3.0.

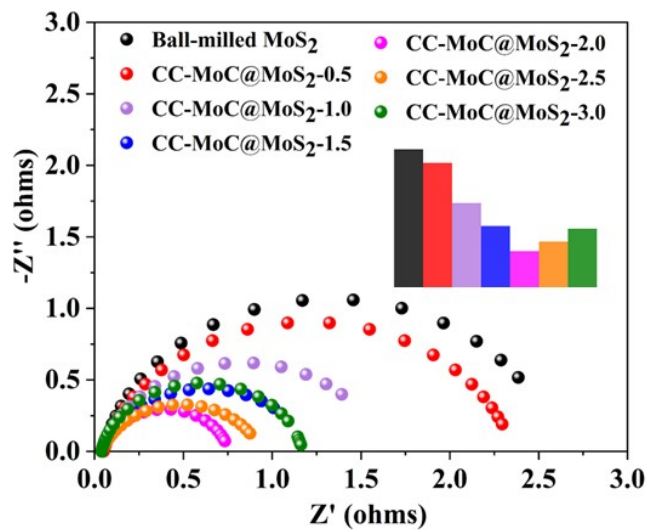


**Fig. S12** The Nyquist plots of BM-MoS<sub>2</sub>, CC-MoC@MoS<sub>2</sub>-0.5, CC-MoC@MoS<sub>2</sub>-1.0, CC-MoC@MoS<sub>2</sub>-1.5, CC-MoC@MoS<sub>2</sub>-2.0, CC-MoC@MoS<sub>2</sub>-2.5 and CC-MoC@MoS<sub>2</sub>-3.0.

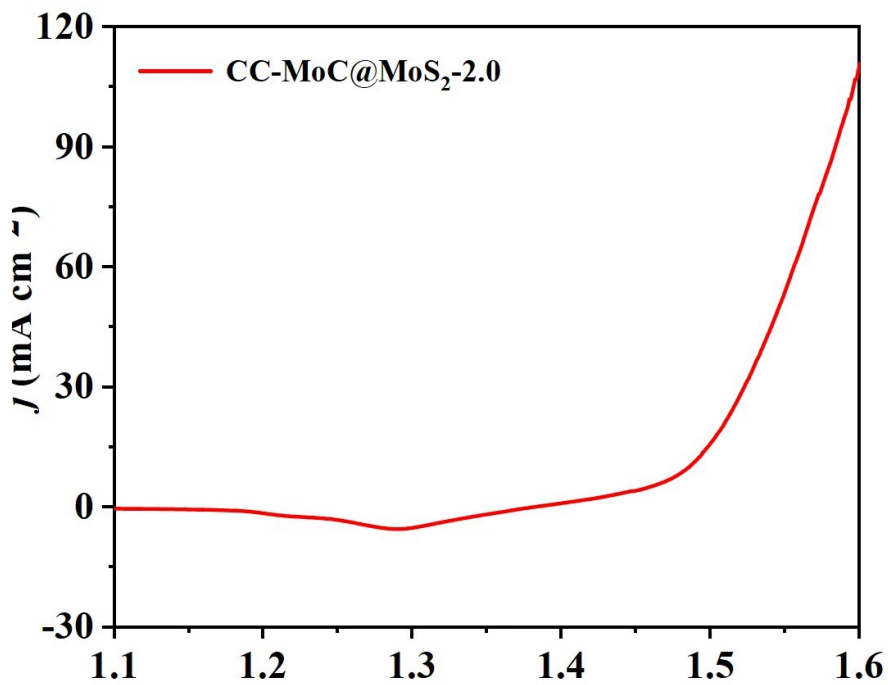


**Fig. S13 LSV curve of CC-MoC@MoS<sub>2</sub>-2.0 after a continuous CV of 5000 cycles.**

**Table S3:** The  $\eta_{10}$ , Tafel slope,  $C_{dl}$  and  $R_{ct}$  values for OER of BM-MoS<sub>2</sub> and CC-MoC@MoS<sub>2</sub>-X catalysts.

Catalysts	$\eta_{10}$ (mV)	Tafel slope (mV dec <sup>-1</sup> )	$C_{dl}$ (mF cm <sup>-2</sup> )	$R_{ct}$ ( $\Omega$ )
Ball-milled MoS <sub>2</sub>	285	112.12	2.98	2.553
CC-MoC@MoS <sub>2</sub> -0.5	268	110.08	3.06	2.309
CC-MoC@MoS <sub>2</sub> -1.0	262	91.22	3.25	1.586
CC-MoC@MoS <sub>2</sub> -1.5	260	86.31	3.25	1.176
CC-MoC@MoS <sub>2</sub> -2.0	248	47.09	4.02	0.716
CC-MoC@MoS <sub>2</sub> -2.5	275	60.48	3.74	0.898
CC-MoC@MoS <sub>2</sub> -3.0	257	79.56	3.08	1.131

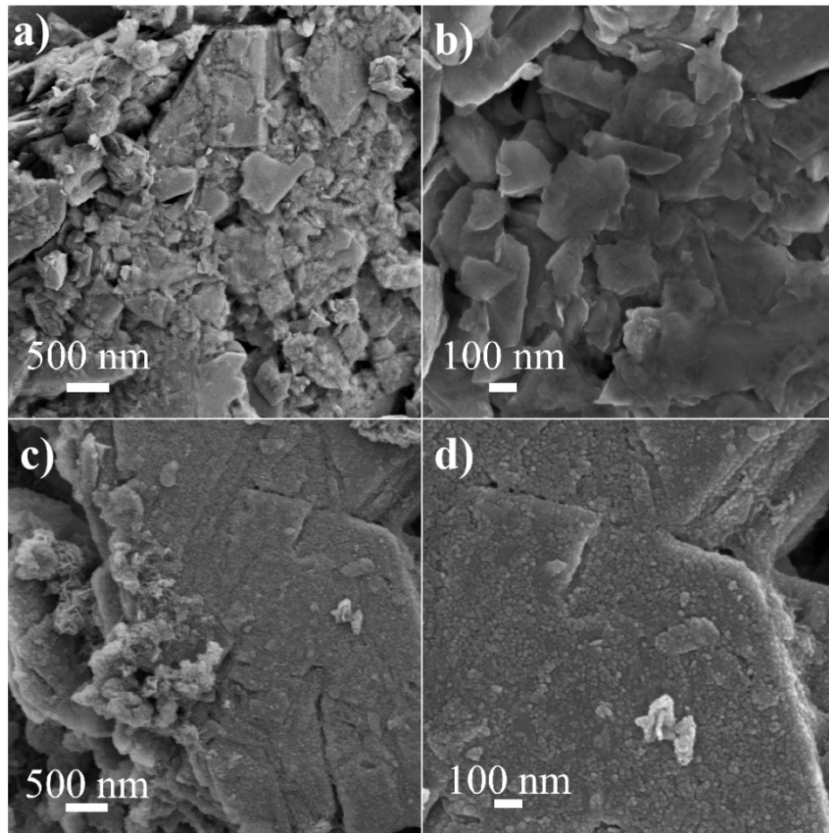


**Fig. S14** SEM images of CC-MoC@MoS<sub>2</sub>-2.0 (a, b) before and (c, d) after stability test.

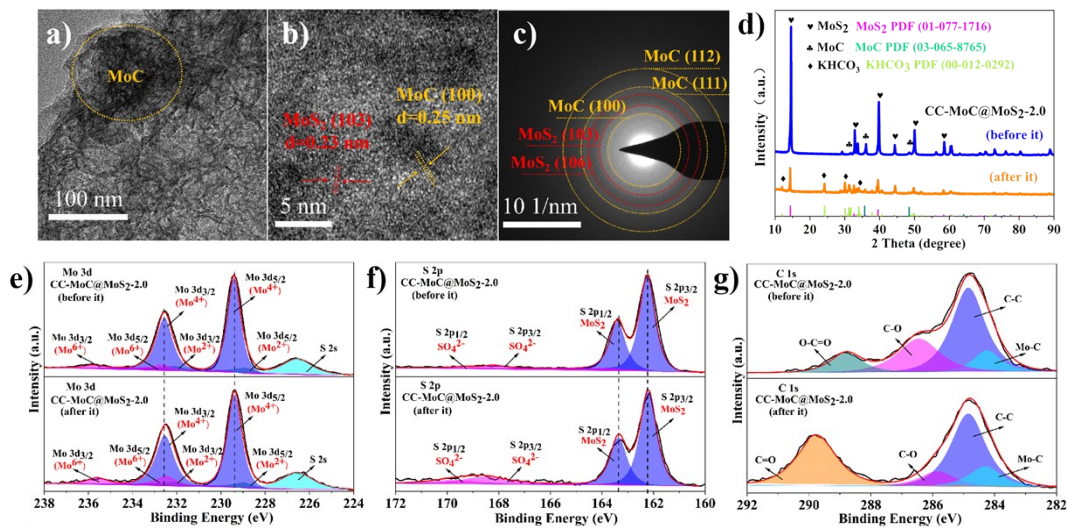


**Fig. S15** (a, b) TEM images and (c) SAED pattern of CC-MoC@MoS<sub>2</sub>-2.0 after stability test. (d) XRD patterns and XPS spectra of (e) Mo 3d, (f) S 2p, (g) C 1s of CC-MoC@MoS<sub>2</sub>-2.0 before and after stability test.

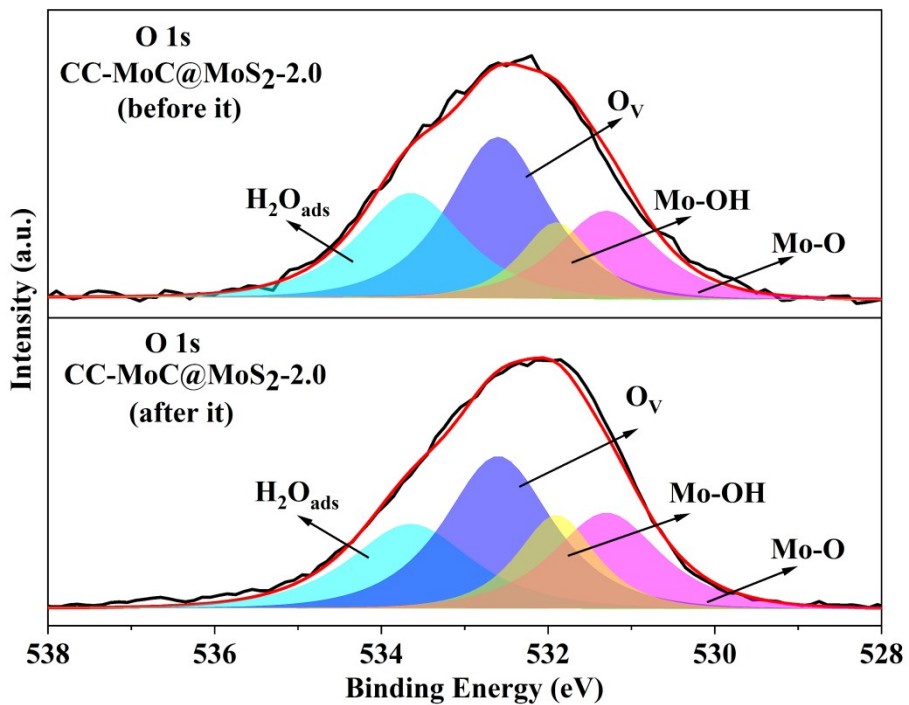


**Fig. S16** High-resolution XPS spectra of O 1s of CC-MoC@MoS<sub>2</sub>-2.0 before and after stability test.

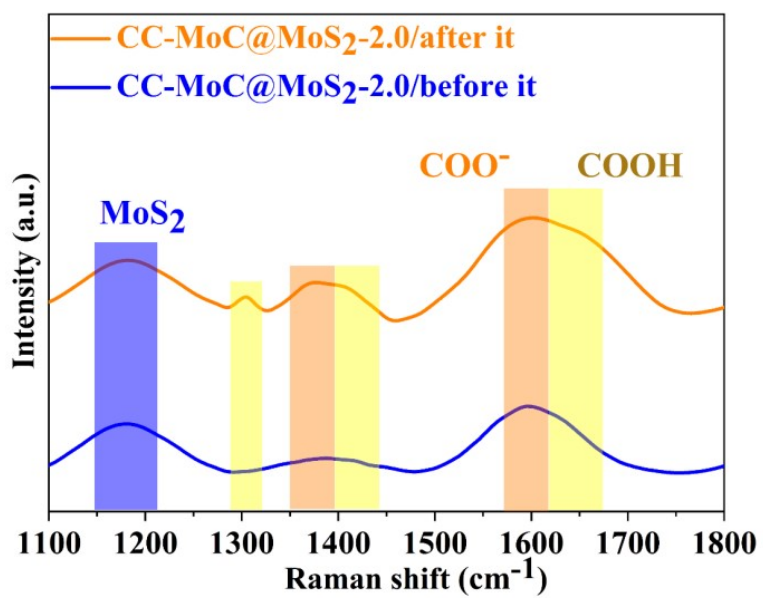


**Fig. S17** Raman spectra of CC-MoC@MoS<sub>2</sub>-2.0 before and after stability test.

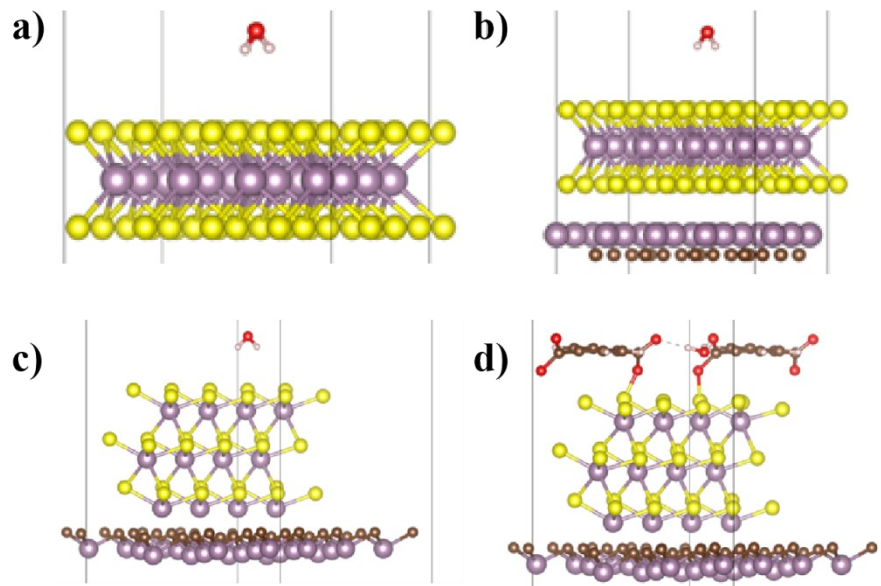


**Fig. S18** Water adsorption models of (a) MoS<sub>2</sub>, (b) MoC@MoS<sub>2</sub>-I, (c) MoC@MoS<sub>2</sub>-II and (d) CC-MoC@MoS<sub>2</sub>-2.0.

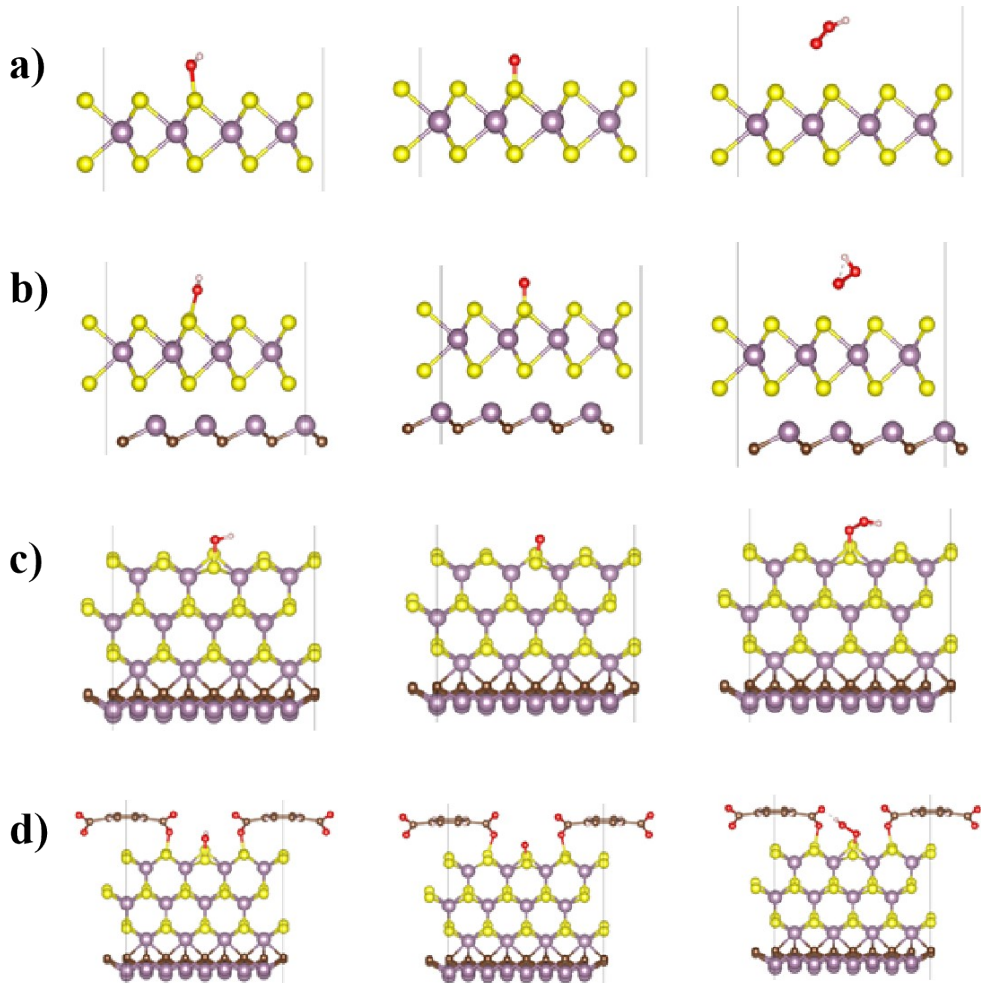


**Fig. S19** Theoretical structural models of clean surfaces and  $^*\text{OH}$ ,  $^*\text{O}$ ,  $^*\text{OOH}$  intermediates adsorbed on the surfaces of a)  $\text{MoS}_2$ , b)  $\text{MoC}@\text{MoS}_2\text{-I}$ , c)  $\text{MoC}@\text{MoS}_2\text{-II}$  and d)  $\text{CC-MoC}@\text{MoS}_2$ .

**Table S4:** The calculated  $E^*$ (eV), Gibbs free energy change  $\Delta_r G$ (eV) and theoretical overpotential  $\eta$ (eV) values of the OER performance (calibration at 298.15 K, the unit of physical quantity is eV, U = 0 V).

System	$E^*$	$G_{\text{H}_2\text{O}}$	$G_{\text{H}_2}$	$G_{\text{O}_2}$	$\Delta_r G_1$	$\Delta_r G_2$	$\Delta_r G_3$	$\Delta_r G_4$	$\eta$
$\text{MoS}_2$	-364.73				1.40	-	-	-	-
$\text{MoC}@\text{MoS}_2\text{-I}$	-661.31				1.11	-	-	-	-
$\text{MoC}@\text{MoS}_2\text{-II}$	-696.01	-14.22	-6.80	-9.92	-0.47	-0.26	1.03	-0.30	1.03
$\text{CC-MoC}@\text{MoS}_2\text{-2.0}$	-809.10				-0.11	-0.53	0.94	-0.30	0.94

**Table S5:** The energies of proton generation and migration of different electrocatalysts calculated by CI-NEB method.

System	Reaction	$E_{\text{transition}}$ (eV)
MoC@MoS <sub>2</sub> -II		0.47
	Proton generation	
CC-MoC@MoS <sub>2</sub>		0.42
MoC@MoS <sub>2</sub> -II		0.84
	Proton transfer	
CC-MoC@MoS <sub>2</sub>		0.72

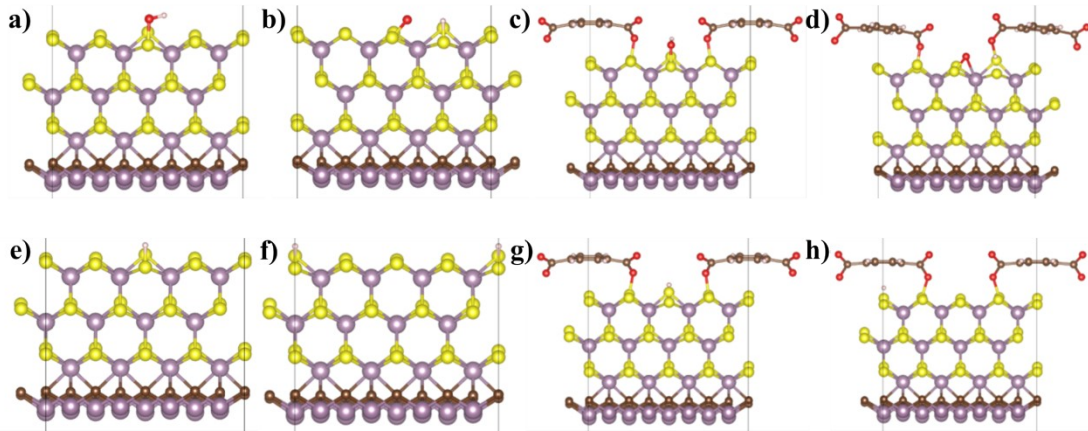


**Fig. S20** Schematic illustration of the proposed proton transfer processes of MoC@MoS<sub>2</sub>-II and CC-MoC@MoS<sub>2</sub>-2.0. The initial and final proton generation states of MoC@MoS<sub>2</sub>-II (a, b) and CC-MoC@MoS<sub>2</sub>-2.0 (c, d). The initial and final states of proton migration of MoC@MoS<sub>2</sub>-II (e, f) and CC-MoC@MoS<sub>2</sub>-2.0 (g, h).

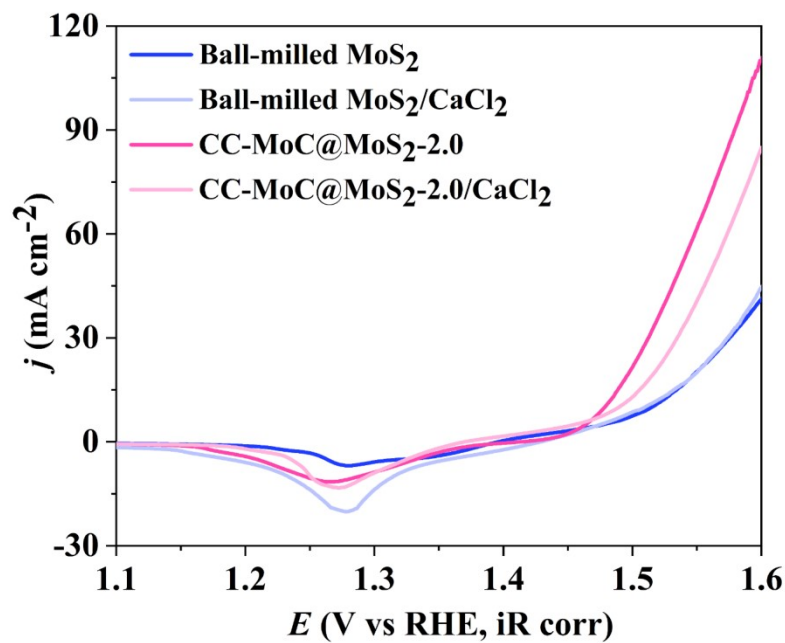


**Fig. S21** LSV curves of BM-MoS<sub>2</sub> and CC-MoC@MoS<sub>2</sub>-2.0 with and without CaCl<sub>2</sub> in the electrolyte.

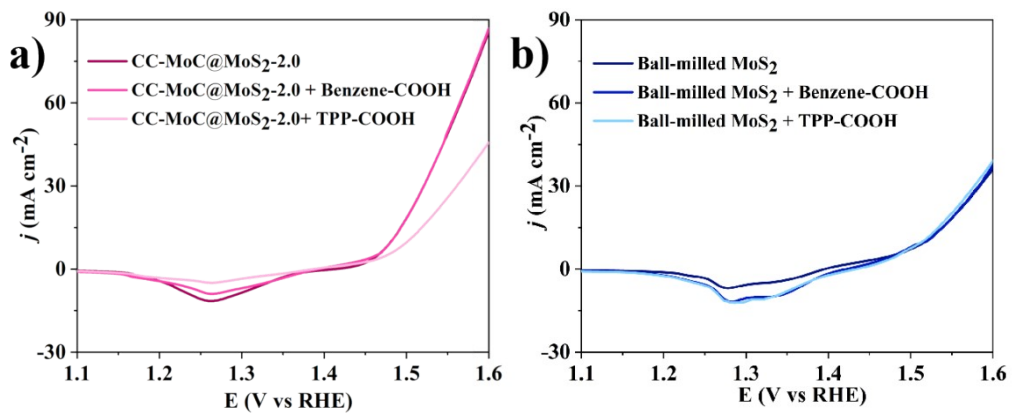


**Fig. S22** LSV curves of (a) CC-MoC@MoS<sub>2</sub>-2.0 and (b) BM-MoS<sub>2</sub> catalysts in 1 M KOH with the titration of 5 mM TPP-COOH or Benzene-COOH.

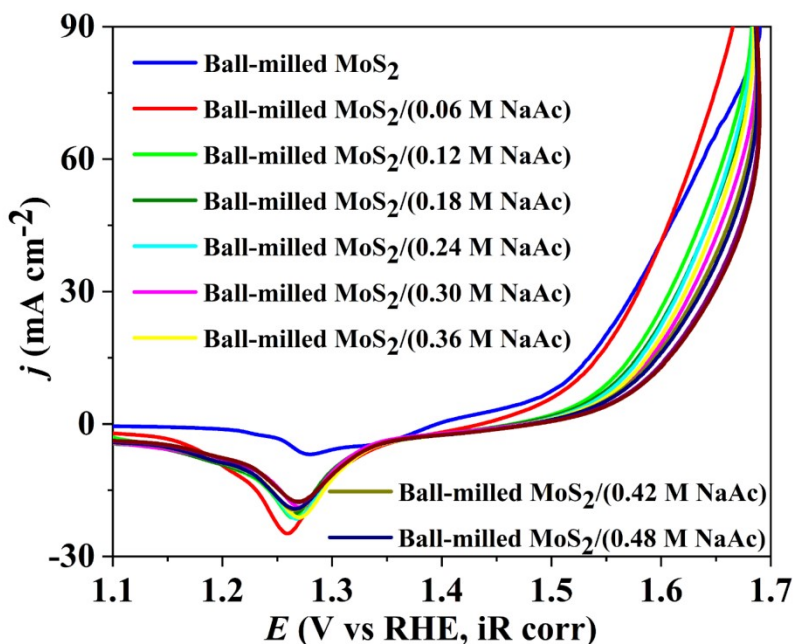


**Fig. S23** LSV curves of BM-MoS<sub>2</sub> catalysts in 1 M KOH with NaAc solutions of different concentrations.

## References

- [1] Y.Luo, H.Yang, P.Ma, S.Luo, Z.Zhao, J.Ma, Fe<sub>3</sub>O<sub>4</sub>/CoO interfacial nanostructure supported on carbon nanotubes as a highly efficient electrocatalyst for oxygen evolution reaction, ACS Sustainable Chem. Eng. 8 (2020)3336-3346.
- [2] Y.Zuo, D.Rao, S.Ma, T.Li, Y. H.Tsang, S.Kment, Y.Chai, Valence engineering via dual-cation and boron doping in pyrite selenide for highly efficient oxygen evolution, ACS Nano 13(2019)11469-11476.
- [3] X. Wang, Y.Zheng, J.Yuan, J.Shen, J.Hu, A.j.Wang, L.Wu, L.Niu, Porous NiCo diselenide nanosheets arrayed on carbon cloth as promising advanced catalysts used in water splitting, Electrochim. Acta 225(2017) 503-513.
- [4] G.Wu, W.X.Chen,X.S. Zheng,D.P. He,Y.Q. Luo, X.Q.Wang, J.Yang, Y.E.Wu, W.S.Yan, Z.B.Zhuang, X.Hong,Y.D. Li, Hierarchical Fe-doped NiO<sub>X</sub> nanotubes assembled from ultrathin nanosheets containing trivalent nickel for oxygen evolution reaction, Nano Energy 38(2017)167-174.
- [5] L.A.Stern, L.Feng, F.Song, X.Hu, Ni<sub>2</sub>P as a Janus catalyst for water splitting: the oxygen evolution activity of Ni<sub>2</sub>P nanoparticles, Energy Environ. Sci. 8(2015)2347-2351.
- [6] G. Zeng, M.Liao, C.Zhou, X.Chen, Y.Wang, D.Xiao, Iron and nickel co-doped cobalt hydroxide nanosheets with enhanced activity for oxygen evolution reaction,RSC Adv.6(2016)42255-42262.
- [7] X.Xiong, Y.Ji, M.Xie, C.You, L.Yang, Z.Liu, A. M. Asiri, X.Sun, MnO<sub>2</sub>-CoP<sub>3</sub> nanowires array: an efficient electrocatalyst for alkaline oxygen evolution reaction with enhanced activity, Electrochim. Commun. 86(2018)161-165.
- [8] Y.Zhao, J.Zhang, X.Guo, H.Fan, W.Wu, H.Liu, G.Wang, Fe<sub>3</sub>C@Nitrogen doped CNT arrays

aligned on nitrogen functionalized carbon nanofibers as highly efficient catalysts for the oxygen evolution reaction, *J. Mater. Chem. A* 5(2017) 19672-19679.

- [9] J.Du, T.Zhang, J.Xing, C.Xu, Hierarchical porous  $\text{Fe}_3\text{O}_4/\text{Co}_3\text{S}_4$  nanosheets as an efficient electrocatalyst for the oxygen evolution reaction, *J. Mater. Chem. A* 5(2017)9210-9216.
- [10] D. C.Nguyen, T. L.Luyen Doan, S.Prabhakaran, D. T.Tran, D. H.Kim, J. H.Lee, N. H.Kim, Hierarchical Co and Nb dual-doped  $\text{MoS}_2$  nanosheets shelled micro- $\text{TiO}_2$  hollow spheres as effective multifunctional electrocatalysts for HER, OER, and ORR, *Nano Energy* 82(2021)105750.
- [11]Z.Lu, L.Qian, Y.Tian, Y.Li, X.Sun, X.Duan, Ternary NiFeMn layered double hydroxides as highly-efficient oxygen evolution catalysts, *Chem.Comm.* 52(2016)908-911.
- [12]J.G.Li, K.Xie, H.Sun, Z.Li, X.Ao, Z.Chen, K. K.Ostrikov, C.Wang, W.Zhang, Template-directed bifunctional dodecahedral  $\text{CoP/CN@MoS}_2$  electrocatalyst for high efficient water splitting, *ACS Appl. Mater. Interfaces* 11(2019)36649-36657.
- [13]T.Huang, Y.Chen, J.M.Lee, A microribbon hybrid structure of  $\text{CoO}_x\text{-MoC}$  encapsulated in N-doped carbon nanowire derived from MOF as efficient oxygen evolution electrocatalysts. *Small* 13(2017) 1702753.
- [14]S.Zhang, Y.Sun, F.Liao, Y.Shen, H.Shi, M.Sha,  $\text{Co}_9\text{S}_8\text{-CuS-FeS}$  trimetal sulfides for excellent oxygen evolution reaction electrocatalysis, *Electrochim. Acta* 283(2018)1695-1701.
- [15]. C.Lee, K.Shin, C.Jung, P.P.Choi, G.Henkelman, H. M.Lee, Atomically embedded Ag via electrodiffusion boosts oxygen evolution of  $\text{CoOOH}$  nanosheet arrays, *ACS Catal.* 10(2020) 562-569.
- [16] J.Chen, H.Zhang, B.Li, J.Yang, X.Li, T.Zhang, C.He, C.Duan, L.Wang, Bioinspired carboxylate-water coordination polymers with hydrogen-bond clusters and local coordination flexibility for electrochemical water splitting, *ACS Appl. Energy Mater.* 3(2020) 10515-10524.
- [17]Y.J.Tang, C.H. Liu, W.Huang, X.L Wang, L.Z.Dong, S.L.Li, Y.Q.Lan, Bimetallic carbides-based nanocomposite as superior electrocatalyst for oxygen evolution reaction, *ACS Appl. Mater. Interfaces* 9(2017)16977-16985.